Astronomy & Astrophysics

Depletion of chlorine into HCl ice in a protostellar core

The CHESS spectral survey of OMC-2 FIR 4[*]

M. Kama[1], E. Caux[2,3], A. López-Sepulcre[4,5], V. Wakelam[6,7], C. Dominik[8,9], C. Ceccarelli[4,5], M. Lanza[10], F. Lique[10], B. B. Ochsendorf[1], D. C. Lis[11,12,13], R. N. Caballero[14], and A. G. G. M. Tielens[1]

[1] Leiden Observatory, PO Box 9513, 2300 RA Leiden, The Netherlands
    e-mail: mkama@strw.leidenuniv.nl
[2] Université de Toulouse, UPS-OMP, IRAP, Toulouse, France
[3] CNRS, IRAP, 9 Av. colonel Roche, BP 44346, 31028 Toulouse Cedex 4, France
[4] Université de Grenoble Alpes, IPAG, 38000 Grenoble, France
[5] CNRS, IPAG, 38000 Grenoble, France
[6] Univ. Bordeaux, LAB, UMR 5804, 33270 Floirac, France
[7] CNRS, LAB, UMR 5804, 33270 Floirac, France
[8] Astronomical Institute Anton Pannekoek, Science Park 904, 1098 XH Amsterdam, The Netherlands
[9] Department of Astrophysics/IMAPP, Radboud University Nijmegen, Nijmegen, The Netherlands
[10] LOMC – UMR 6294, CNRS-Université du Havre, 25 rue Philippe Lebon, BP 1123, 76063 Le Havre Cedex, France
[11] LERMA, Observatoire de Paris, PSL Research University, CNRS, UMR 8112, 75014, Paris, France
[12] Sorbonne Universités, Université Pierre et Marie Curie, Paris 6, CNRS, Observatoire de Paris, UMR 8112, LERMA, Paris, France
[13] California Institute of Technology, Cahill Center for Astronomy and Astrophysics 301-17, CA 91125, Pasadena, USA
[14] Max-Planck-Institut für Radioastronomie, Auf dem Hügel 69, 53121 Bonn, Germany

ABSTRACT

Context. The freezeout of gas-phase species onto cold dust grains can drastically alter the chemistry and the heating-cooling balance of protostellar material. In contrast to well-known species such as carbon monoxide (CO), the freezeout of various carriers of elements with abundances $<10^{-5}$ has not yet been well studied.
Aims. Our aim here is to study the depletion of chlorine in the protostellar core, OMC-2 FIR 4.
Methods. We observed transitions of HCl and H_2Cl^+ towards OMC-2 FIR 4 using the *Herschel* Space Observatory and Caltech Submillimeter Observatory facilities. Our analysis makes use of state of the art chlorine gas-grain chemical models and newly calculated HCl-H_2 hyperfine collisional excitation rate coefficients.
Results. A narrow emission component in the HCl lines traces the extended envelope, and a broad one traces a more compact central region. The gas-phase HCl abundance in FIR 4 is 9×10^{-11}, a factor of only 10^{-3} that of volatile elemental chlorine. The H_2Cl^+ lines are detected in absorption and trace a tenuous foreground cloud, where we find no depletion of volatile chlorine.
Conclusions. Gas-phase HCl is the tip of the chlorine iceberg in protostellar cores. Using a gas-grain chemical model, we show that the hydrogenation of atomic chlorine on grain surfaces in the dark cloud stage sequesters at least 90% of the volatile chlorine into HCl ice, where it remains in the protostellar stage. About 10% of chlorine is in gaseous atomic form. Gas-phase HCl is a minor, but diagnostically key reservoir, with an abundance of $\lesssim 10^{-10}$ in most of the protostellar core. We find the $[^{35}Cl]/[^{37}Cl]$ ratio in OMC-2 FIR 4 to be 3.2 ± 0.1, consistent with the solar system value.

Key words. stars: formation – astrochemistry – ISM: abundances

1. Introduction

The freezeout and desorption of volatiles are amongst the key factors that determine the gas-phase abundances of chemical species in interstellar gas, in particular in protostellar cores (e.g. Bergin & Langer 1997; Caselli & Ceccarelli 2012). The classical example is CO, which is strongly depleted in prestellar cores, but returns to the gas in the warm protostellar stages Class 0 and I (e.g. Caselli et al. 1999; Bacmann et al. 2002; Jørgensen et al. 2005). Similar behaviour, with quantitative differences, is seen or expected for many other species. Here, we investigate the freezeout and main reservoirs of chlorine in a protostellar core.

An ice mantle on a dust grain in a protostellar core mainly consists of a few dominant ice species (e.g. H_2O, CO, CO_2, CH_3OH). However, the ices also contain a large number of minor species, accreted from the gas and formed in the ice matrix. Such minor species very likely include HF and HCl, which are the main molecular carriers of the halogen elements fluorine and chlorine, in well-shielded molecular gas. With increasing temperature, such as seen during infall towards a central protostar, the ice mantle desorbs. For any given ice species, the desorption may have multiple stages, with details influenced by its abundance and interaction with the other species in the ice (Collings et al. 2004; Lattelais et al. 2011). In the hot cores of protostars, where ice mantles largely desorb, most volatile species are expected to be back in the gas phase.

We study the depletion of volatile chlorine towards the OMC-2 FIR 4 protostellar core, using HCl and H_2Cl^+ as proxies.

---

[*] Appendices are available in electronic form at http://www.aanda.org

We employed the *Herschel* Space Observatory[1] and the Caltech Submillimeter Observatory (CSO) telescopes and made use of both an updated gas-grain chemical network for chlorine and new calculations of the HCl-H_2 hyperfine collisional excitation rate coefficients. In Sect. 2, we review the interstellar chemistry of chlorine. The source is described in Sect. 3 and the observations in Sect. 4. The analysis separately covers HCl (Sect. 5) and H_2Cl^+ (Sect. 6), and the results are discussed in Sect. 7. We present our conclusions in Sect. 8.

2. Interstellar chlorine chemistry

Chlorine has a simple and relatively well characterized interstellar chemistry (e.g. Jura 1974; Dalgarno et al. 1974; Blake et al. 1986; Schilke et al. 1995; Neufeld & Wolfire 2009). In dense molecular gas, the gas-phase formation of HCl begins with the reaction

$$Cl + H_3^+ \rightarrow H_2Cl^+ + H. \qquad (1)$$
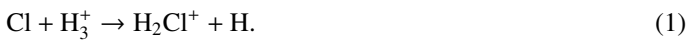
Dissociative recombination of H_2Cl^+ with e^- then produces HCl. A recent study of D_2Cl^+ has confirmed the branching ratio of this recombination to be ~10% into HCl, ~90% into Cl (Novotný et al. 2012). Below ~100 K, the resulting fraction of chlorine in HCl is ~0.1 to 0.3 (Dalgarno et al. 1974; Blake et al. 1986; Schilke et al. 1995; Neufeld & Wolfire 2009). At temperatures of $\gtrsim 350$ K, all chlorine can be converted into HCl in dense ($n \gtrsim 10^4$ cm^{-3}) molecular gas by the reaction

$$Cl + H_2 \rightarrow HCl + H, \qquad (2)$$

on a timescale of $\lesssim 10^4$ yr. At colder temperatures, this reaction is much slower.

In photon-dominated regions (PDRs), a layer can form where the reactions $Cl^+ + H_2 \rightarrow HCl^+ + H$ and $HCl^+ + H_2 \rightarrow H_2Cl^+ + H$ lead again via dissociative recombination to HCl. In diffuse PDRs ($n_H \sim 10^3$ cm^{-3}), the HCl and H_2Cl^+ column density ratio is ~1, while for 10^7 cm^{-3} it is ~10^2 (Neufeld & Wolfire 2009). At $A_V \lesssim 1$ however, the ratio can be ~0.01, while atomic Cl is the dominant gas-phase reservoir of chlorine. At low densities and $A_V \ll 1$, Cl^+ dominates.

The abundance of Cl with respect to atomic hydrogen in the solar photosphere is [Cl]/[H] = 3.16×10^{-7} (Asplund et al. 2009). The meteoritic abundance is 1.8×10^{-7} (Lodders 2003), while in the diffuse interstellar medium (ISM) it is 10^{-7}, indicating a factor of two depletion into refractory grains or volatile ices (Moomey et al. 2012). For our modelling, we refer to the abundance with respect to molecular hydrogen, X(Cl) = [Cl]/[H_2], and adopt a reference value X(Cl) = 10^{-7}.

The main stable isotopes of chlorine are ^{35}Cl and ^{37}Cl. Their ratio in the solar system is 3.1 (Lodders 2003).

3. The FIR 4 protostellar core

Our target is a nearby intermediate-mass protostellar core, OMC-2 FIR 4[2] (hereafter FIR 4), located in Orion, at a distance of $d \approx 420$ pc (Hirota et al. 2007; Menten et al. 2007). Its envelope mass is ~30 $M_\odot$ and its luminosity within ~20″ is ~100 $L_\odot$, while the ~1′ scale envelope has an estimated luminosity of ~ 400–1000 $L_\odot$ (Mezger et al. 1990; Furlan et al. 2014;

Crimier et al. 2009, the latter is hereafter referred to as C09). Class 0 suggests an age of $\lesssim 10^5$ yr, and Furlan et al. (2014) propose that FIR 4 is amongst the youngest protostellar cores known. In the far-infrared to millimetre regimes, FIR 4 is undergoing intense study in the *Herschel* key programmes CHESS (Ceccarelli et al. 2010; Kama et al. 2010, 2013; López-Sepulcre et al. 2013a,b; Ceccarelli et al. 2014) and HOPS (Adams et al. 2012; Manoj et al. 2013; Furlan et al. 2014), as well as in a number of ground-based projects.

The main physical components of FIR 4 are the warm, clumpy inner envelope and the cold, extended outer one; a proposed outflow; and a tenuous, heavily irradiated foreground cloud (Crimier et al. 2009; Kama et al. 2013; López-Sepulcre et al. 2013a,b; Furlan et al. 2014). The inner envelope has been resolved into continuum peaks with different luminosities (Shimajiri et al. 2008; Adams et al. 2012; López-Sepulcre et al. 2013b; Furlan et al. 2014). These sources appear to share a large envelope. The line profiles and excitation of CO and H_2O show that FIR 4 harbours a compact outflow (Kama et al. 2013; Furlan et al. 2014). There are also two PDRs to consider: the dense outermost envelope ($n_{H_2} = 6 \times 10^5$ cm^{-3}, Crimier et al. 2009), and the tenuous foreground cloud ($n_{H_2} \approx 10^2$ cm^{-3}, López-Sepulcre et al. 2013a). Whether or not they are physically connected is unclear. For simplicity, we treat them as separate entities, even though there may be a smooth transition in physical conditions between the two.

4. Observations

The main neutral and ionized molecular carriers of chlorine in the ISM – such as HCl, HCl^+ and H_2Cl^+ – have strong radiative transitions, although their observations from the ground are hampered by atmospheric water absorption. The observations of HCl and H_2Cl^+ towards FIR 4, summarized in Table 1 and shown in Figs. 1 (HCl) and 2 (H_2Cl^+), were carried out with the *Herschel* Space Observatory and the CSO.

4.1. Herschel/HIFI

As part of the CHESS key programme (Ceccarelli et al. 2010), FIR 4 was observed with the Heterodyne Instrument for the Far-Infrared (HIFI) wide band spectrometer (de Graauw et al. 2010) on the *Herschel* Space Observatory (Pilbratt et al. 2010), in Dual Beam Switch (DBS) mode at a resolution of dν = 1.1 MHz ($R \sim 10^6$). Multiple transitions of HCl and H_2Cl^+ were covered. The data quality and reduction, carried out with the HIPE 8.0.1 software (Ott 2010), are presented in Kama et al. (2013).

4.2. Caltech submillimeter observatory

Ground-based observations of HCl J = 1–0 were carried out in DBS mode with a chopper throw of 240″, using the 690 GHz facility heterodyne receiver of the CSO, on Mauna Kea, Hawaii, on February 6th and 11th, 2013. The atmosphere was characterized by a 225 GHz zenith opacity of 0.04–0.06 or 1 mm of precipitable water vapour. Typical single sideband system temperatures were 5000–7000 K. The backend was the high-resolution FFT spectrometer, with 4095 channels over 1 GHz of IF bandwidth. The on-source integration time was 51 min, resulting in an RMS noise of ~0.15 K at a resolution of 3.7 km s^{-1}. Jupiter was used for pointing and calibration. The beam efficiency was 40%, assuming a 148.5 K brightness temperature for Jupiter.

---

[1] *Herschel* is an ESA space observatory with science instruments provided by European-led Principal Investigator consortia and with important participation from NASA.

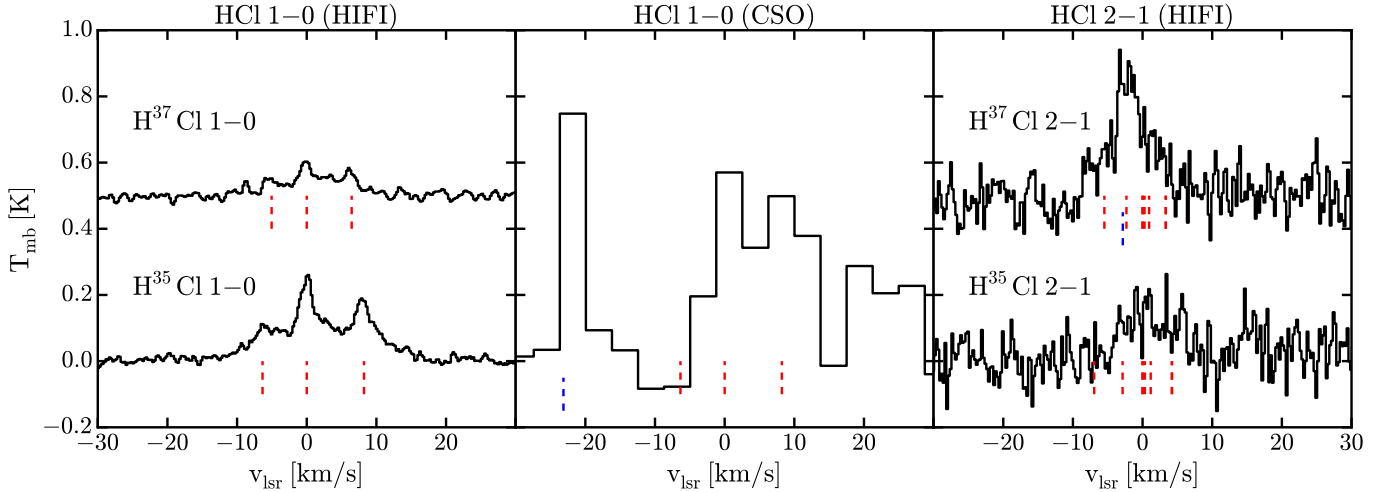[2] Identified on SIMBAD as [MWZ90] OMC-2 FIR 4.

Fig. 1. Observed spectra of HCl from *Herschel*/HIFI and CSO, velocity-corrected and centred on the strongest hyperfine component. Red dashed lines indicate the hyperfine components of the rotational transitions, while blue dashed lines show CH_3OH lines. The CSO data have been binned to $\delta v = 3.7$ km s^{-1}.

Table 1. Summary of the observations.

Transition	Frequency [GHz]	E_u [K]	Telescope	Beam ["]	Flux [K km s^{-1}]	Notes and obsids[*]
			HCl			
1–0	625.9	30.1	HIFI	34	2.79 ± 0.03	1342191591, 1342239639
	625.9	30.1	CSO	11	4 ± 2	–
2–1	1251.5	90.1	HIFI	17	1.46 ± 0.12	1342216386, 1342239641
			$H^{37}Cl$			
1–0	625.0	30.1	HIFI	34	0.88 ± 0.03	1342191591, 1342239639
2–1	1249.5	90.1	HIFI	34	≤2.23	1342216386, 1342239641. Blended with CH_3OH.
			H_2Cl^+			
$1_{1,1}-0_{0,0}$	485.4	23.0	HIFI	44	−0.21 ± 0.02	1342218633
$2_{0,2}-1_{1,1}$	698.6	57.0	HIFI	30	≤0.05	1342216389
$2_{1,2}-1_{0,1}$	781.6	58.0	HIFI	27	−0.62 ± 0.05	1342194681
$2_{2,1}-1_{1,0}$	1159.2	85.0	HIFI	18	≤0.19	1342217735
			$H_2^{37}Cl^+$			
$1_{1,1}-0_{0,0}$	484.2	23.0	HIFI	44	≤0.08	1342218633
$2_{0,2}-1_{1,1}$	698.5	57.0	HIFI	30	≤0.05	1342216389
$2_{1,2}-1_{0,1}$	780.0	58.0	HIFI	27	0.26 ± 0.06	1342194681
$2_{2,1}-1_{1,0}$	1156.0	85.0	HIFI	18	≤0.19	1342217735

Notes. Only lines with a flux signal to noise of ≥5 are given as detections. All uncertainties and limits are at 1σ confidence. Upper limits for H_2Cl^+ are calculated over 5 km s^{-1}. [*] *Herschel* observation identifier.

4.3. Overview of the data

Both HCl and H_2Cl^+, as well as their isotopologs, are detected with *Herschel*/HIFI. The HCl 1−0 transition is also detected with the CSO. The measured line fluxes, integrated over the hyperfine components, are summarized in Table 1.

The HCl lines show evidence for a broad and a narrow component. Both components are present in the HIFI HCl 1–0 data, which also shows a roughly optically thin hyperfine component ratio (2:3:1, in order of increasing v) for the narrow component. The signal to noise of the HCl 2–1 and the CSO 1–0 data are insufficient to make firm conclusions about the relative importance of the broad and narrow components, however the broad component seems to contribute substantially to both observations. Unfortunately, the $H^{37}Cl$ 2–1 transition is contaminated by a CH_3OH transition and is therefore excluded from our analysis.

5. Analysis of HCl

Here, we first disentangle the kinematical components of the hydrogen chloride lines. Then, we use radiative transfer and chemical modelling to determine the gas-phase HCl abundance. The outermost envelope of FIR 4 is strongly externally irradiated, and is considered separately in Sect. 5.4.

5.1. Kinematics

A two-component model of the hyperfine structure in the HCl 1–0 observations strongly constrains the kinematic parameters of the broad and narrow components, given in Table 2.

In Fig. 3, we compare the kinematic components of HCl to those of other species from the FIR 4 HIFI spectrum of Kama et al. (2013). The properties of the narrow component match the large-scale quiescent envelope tracers, such as $C^{18}O$. The broad
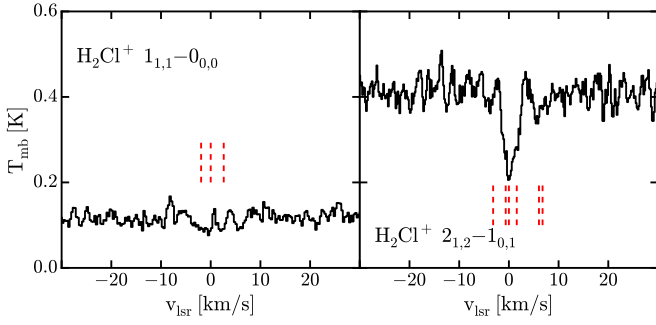
Fig. 2. Observed spectra of H_2Cl^+ from *Herschel*/HIFI. Only the lines formally detected in absorption are shown, and are velocity-corrected and centred on the strongest hyperfine component. Red dashed lines indicate the hyperfine components of the rotational transitions. The continuum has not been subtracted. See also Fig. B.1.
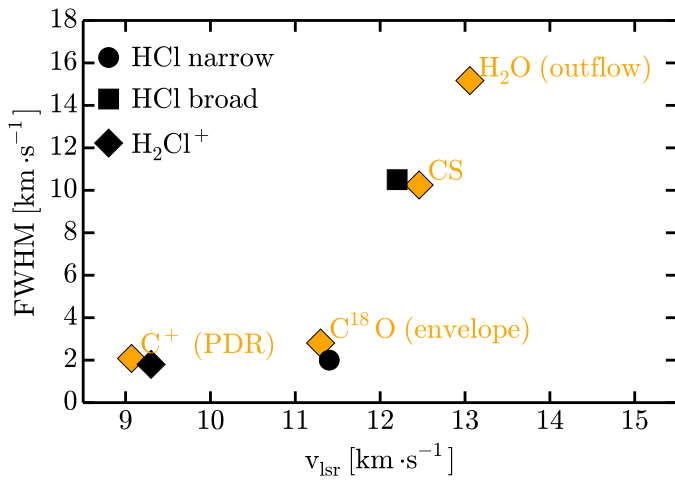

Fig. 3. Kinematical properties of HCl and H_2Cl^+ compared to other species in FIR 4, each of which is annotated with the main physical component it traces. The label "PDR" refers here to the tenuous foreground cloud discovered by López-Sepulcre et al. (2013a). For the comparison species, the mean Gaussian fit parameters from Kama et al. (2013) are plotted.

Table 2. Kinematical properties of the observed HCl line profiles.

Species	Component	v_{lsr} [km s^{-1}]	$FWHM$ [km s^{-1}]
HCl	Narrow	11.4 ± 0.2	2.0 ± 0.2
HCl	Broad	12.2 ± 0.2	10.5 ± 0.5

component parameters lie between those of the envelope and the outflow tracers, and match the mean properties of CS.

Contrary to HCl, for which exceptional observing conditions or space observatories are required, isotopologs of CS are readily observed with ground-based instruments. In Fig. 4, we show a map of the $C^{34}S$ 3–2 line width, based on Plateau de Bure Interferometer data from López-Sepulcre et al. (2013b). A spatially resolved region ~10″ across (2100 AU radius) and detected at a 3σ confidence at $F_{C^{34}S} \geq 0.4$ Jy km s^{-1} beam^{-1} has a line width of $\gtrsim 6$ km s^{-1}. The spatial resolution of the data is ~5″, the channel width is 4 km s^{-1}, and the flux loss compared to single-dish data is ~60%, so we can only conclude that if the $C^{34}S$ broad component is equivalent to that of HCl, the latter is centrally peaked and extended on several thousand AU scales.
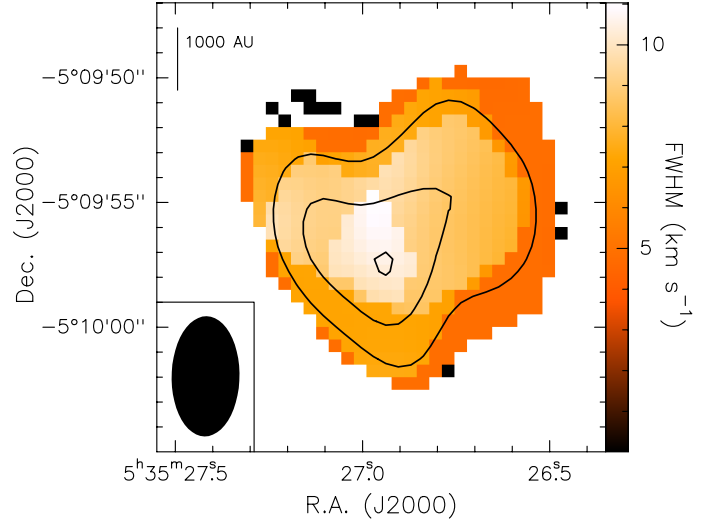
Fig. 4. Line width map of $C^{34}S$ 3–2 (colour map), obtained with the Plateau de Bure Interferometer (López-Sepulcre et al. 2013b). The channel width of the data is 4 km s^{-1}. Overplotted are continuum contours (black lines), which start at 3σ with a 3σ step, with $1\sigma = 0.14$ Jy km s^{-1} beam^{-1}. North is up and east is left.

Based on the arguments presented above, we attribute the narrow and broad HCl line profile component to the outer envelope and some compact yet dynamic inner region, respectively. Given the large difference in line width between the broad HCl component and the outflow tracers CO and H_2O, it is unlikely that they trace the same volumes of gas.

5.2. The gas-phase HCl abundance in FIR 4

To obtain an abundance profile, we modelled the HCl excitation and radiative transfer in FIR 4 using the Monte Carlo code, Ratran[3] (Hogerheijde & van der Tak 2000) as described below.

5.2.1. New HCl-H_2 collisional excitation rates

We modelled the HCl emission using new hyperfine-resolved collisional excitation rate coefficients, presented in detail in Appendix A. These are based upon the recent potential energy surface and rotational excitation rate coefficients of Lanza et al. (2014b,a). In Fig. 6, we compare the new rate coefficients to the HCl-He ones from Neufeld & Green (1994) and Lanza & Lique (2012). The latter, scaled to H_2 collisions by a mass correction factor of 1.38, differ from the new coefficients by a factor of a few at $T_{kin} > 50$ K, and by around a factor of ten at $T_{kin} < 50$ K. A similar difference has been found for HF (Guillon & Stoecklin 2012). We discuss the impact of the new excitation rates on HCl depletion estimates in Sect. 7.5.

5.2.2. The source model

As the basis of our modelling, we adopted the spherically symmetric large-scale source structure with no enhancement of the external irradiation field ($G_0 = 1$ interstellar radiation fields, ISRF) from C09. The density and temperature profiles, as well as the relative populations of the relevant HCl rotational levels, are shown in Fig. 5. Due to the limited spatial resolution of the continuum maps it is based on, the source model is not well
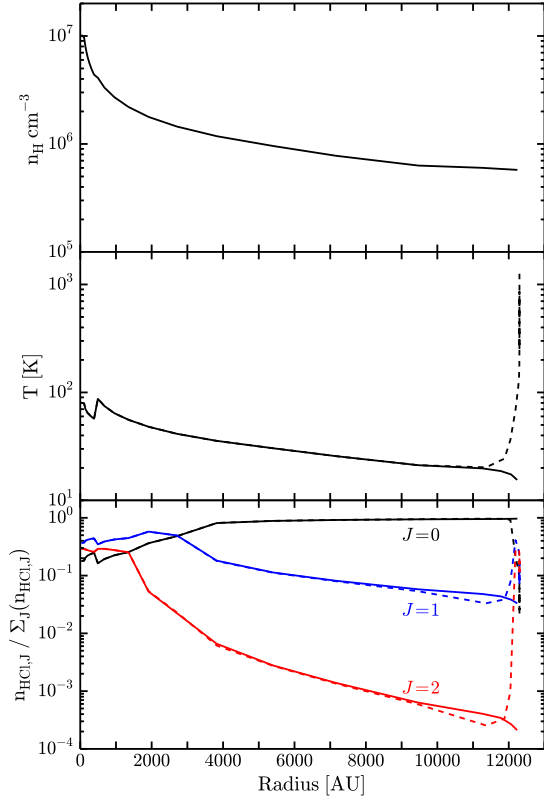

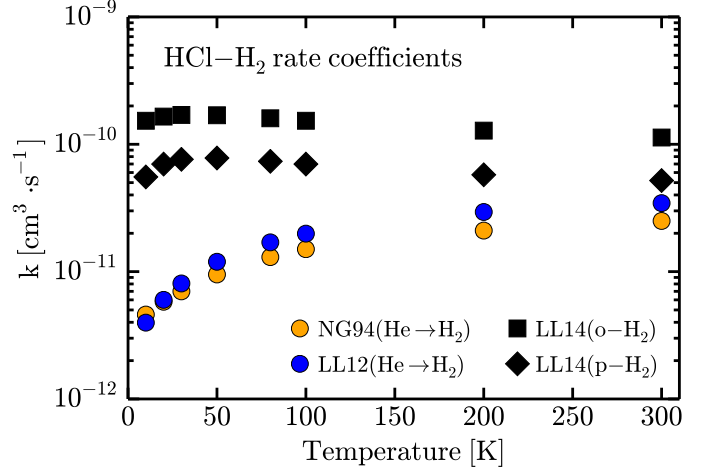[3] http://www.sron.rug.nl/~vdtak/ratran/

Fig. 6. Rate coefficients for the collisional excitation HCl $J = 0 \rightarrow 1$ by H_2. The previously available HCl-He rate coefficients, scaled by 1.38 to account for the reduced mass difference, are from Neufeld & Green (1994, orange circles) and Lanza & Lique (2012, blue circles). The new HCl-ortho-H_2 and -para-H_2 rate coefficients (Appendix A) are shown by black squares and diamonds, respectively.

Fig. 5. *Top and middle panels*: large-scale source structure of FIR 4 (n_{gas} at *top*, T_{gas} at *middle*) from Crimier et al. (2009, C09), corresponding to an integrated luminosity of 1000 $L_\odot$. *Bottom panel*: relative populations of the lowest HCl rotational states, showing $J = 0$ (black), $J = 1$ (blue), and $J = 2$ (red) for the C09 source structure without modification (solid lines) and with an added external irradiation of $G_0 = 415$ ISRF (dashed lines; Sect. 5.4). The level populations were modelled with Ratran using the new hyperfine collision rate coefficients presented in Appendix A.

constrained on scales $\lesssim 2000$ AU. Thus, we interpret it as the spherically-averaged large-scale structure of the source. The total H_2 column density in a pencil beam through the centre of the source model is $N(H_2) = 4.6 \times 10^{23}$ cm^{-2}.

According to the relative level populations shown in Fig. 5, the $J_u = 1$ state is most relevant within ~4000 AU, with a factor of five to ten decrease at larger radii, while the $J_u = 2$ state is mostly populated in the inner ~2000 AU and plays no role in the outer envelope. If an external irradiation field is added (Sect. 5.4), the gas temperature reaches ~1000 K in a thin outer layer, and the $J = 2$ and higher level population gains in importance. Thus, the HCl 2–1 line constrains the abundance within 2000 AU and more weakly in a thin outer layer, while the 1–0 transition constrains it in the bulk of the envelope.

5.2.3. Fitting a constant abundance profile

As a first guess, we assume a constant HCl abundance in the source. Assuming a fixed source structure, the model has only two free parameters: X_c, the gas-phase HCl abundance; and R_{bn}, the radius where the line width switches from broad to narrow. We performed a χ^2 minimization on the HCl 1–0 and 2–1 line profiles from HIFI, and the 1–0 from CSO. The best fit parameters, with a reduced $\chi^2 = 1.45$, are $X_c = 9 \times 10^{-11}$ and $R_{bn} = 7000$ AU. In Fig. 7, we show the data, the best-fit model

and the range of models within reduced $\chi^2 = 3$. The $\log_{10}(\chi^2)$ surface is shown in Fig. 8.

5.3. A full chemical model

We modelled the chlorine chemistry at each radial location in FIR 4 with the Nautilus gas-grain chemical code. Nautilus time-dependently computes the gas and grain chemistry including freezeout, surface chemistry, and desorption due to thermal and indirect processes. The grain surface reactions are described in Hersant et al. (2009) and Semenov et al. (2010). The binding energy of Cl on H_2O ice is 1100 K, for HCl we adopted 5174 K from Olanrewaju et al. (2011). The gas-phase network is based on `kida.uva.2011`, from Wakelam et al. (2012), and was updated with data from Neufeld & Wolfire (2009). The full network contains 8335 reactions, 684 species and 13 elements. The H_2 and CO self shielding are computed following Lee et al. (1996), as described in Wakelam et al. (2012). We adopted a volatile chlorine abundance of 10^{-7}. The chemistry is first evolved to steady state in dark cloud conditions. This yields the initial abundances for the time-dependent chemistry in FIR 4, using the C09 source structure for the density and temperature.

Dark cloud stage. The initial conditions for the FIR 4 calculation are computed for dense, cold cloud conditions: a temperature of 10 K, $n_H = 2 \times 10^4$ cm^{-3}, $A_v = 10$ mag, and a cosmic-ray ionization rate of $\zeta = 10^{-17}$ s^{-1}. The model is evolved to 10^6 yr. The species are initially all atomic, except for H_2, with most abundances from Hincelin et al. (2011). The abundance of oxygen is set to 3.3×10^{-4}, and of chlorine to 10^{-7}. At the end of the dark cloud stage, about 93% of elemental chlorine is in HCl ice, the remaining 7% is almost entirely in gas-phase atomic Cl. The temperature, the density and the age of the cloud influence the fraction of Cl and HCl in the gas versus in the ices, but do not affect the HCl/Cl ratio. This ratio, both in the gas and ices, is mostly influenced by the cosmic ray ionization rate ζ. The resulting abundances are used as the initial conditions for FIR 4.

Protostellar stage. For the protostellar stage, we use the C09 density and temperature structure without enhanced external
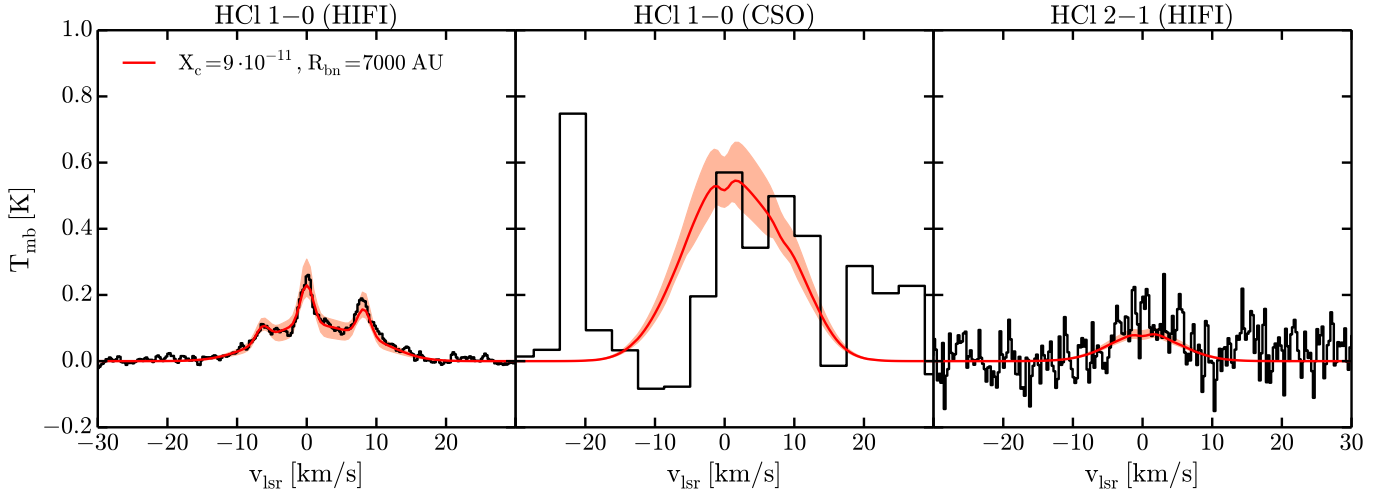
Fig. 7. HCl 1–0 and 2–1 transitions as observed with HIFI and CSO (black). Overplotted are the best-fit constant HCl abundance model (red), and the reduced $\chi^2 < 3$ range (shaded orange) of the models. The strongest feature in the CSO data, at -20 km s^{-1}, is a CH$_3$OH line.
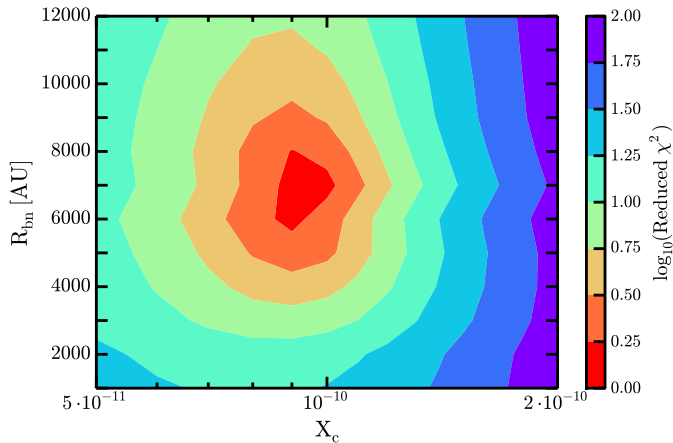

Fig. 8. $\log_{10}$ (reduced χ^2) surface for the two constant HCl abundance model parameters: X_c and R_{bn}.

irradiation. The outermost envelope is treated in more detail in Sect. 5.4. In Fig. 9, we show the gas and ice abundances of HCl and atomic Cl in FIR 4, as modelled with Nautilus at ages 10^4 and 10^5 yr. The trial cosmic ray ionization rates were 10^{-16} s^{-1} (left panel; a foreground cloud value from López-Sepulcre et al. 2013a) and 10^{-14} s^{-1} (right panel; recently inferred for FIR 4 by Ceccarelli et al. 2014).

As seen from the blue lines in Fig. 9, HCl ice is the main reservoir of elemental chlorine outside of $\sim$5000 AU at both times in both models. It stores 90 to 98% of all elemental chlorine. The second reservoir is gaseous atomic chlorine, at 1 to 10% of the elemental total, typically an order of magnitude above the gas-phase HCl abundance. Inside 5000 AU, HCl ice contains 90% ($\zeta = 10^{-16}$ s^{-1}) or 20% ($\zeta = 10^{-14}$ s^{-1}) of the chlorine. The HCl ice is built up over the 10^6 year cold dark cloud stage. The gas-phase HCl abundance slowly decreases with time in most of the source, due to continuing freezeout.

Above, the physical structure switched instantly from the dark cloud structure to the protostellar core. Adding time dependency to the density structure would decrease the abundance changes in the inner envelope, which would be replenished with pristine material from the outer envelope. Additionally, using a

higher prestellar core density would lead to even stronger and more rapid freezeout of chlorine into HCl ice, increasing the depletion.

The gas-phase abundance of HCl from Nautilus is consistent with the observational constraints on $X(HCl)_{gas}$, as reported in Sect. 5.2, within a factor of a few. This is with the exception of the high-ionization model, where $X(HCl)_{gas}$ exceeds the observed limit by two orders of magnitude. The gas-phase HCl abundance of $\sim 10^{-10}$ – seen in most of the source in both models – is the tip of the iceberg, as 90% of all chlorine is frozen onto grain surfaces as HCl and likely in a water ice matrix.

5.4. The outermost envelope PDR

The dense and heavily irradiated photon dominated region in the outermost envelope requires a specialized treatment. We employ the Meudon[4] PDR code (Le Petit et al. 2006) for this. The physical structure is a slab with a constant density of $n_H = 6 \times 10^5$ – the outermost density in the C09 source model – extending to $A_V = 20$ mag. We used two cosmic ray ionization rates, as before: $\zeta = 10^{-16}$ s^{-1} and 10^{-14} s^{-1}.

The external irradiation of FIR 4 has previously been inferred to be $G_0 \sim 500$ interstellar radiation field units, based on [CII] 158 μm emission (Herrmann et al. 1997). We re-evaluated G_0 using the *Herschel*/HIFI [CII] line flux from Kama et al. (2013), which was obtained at higher spatial resolution and yields $G_0 \sim 300$. We further checked G_0 based on an archival *Spitzer* 8 μm map, which has a substantial contribution from PAH emission, and this directly counts excitation events by ultraviolet photons. The measured flux density of $\sim$250 MJy/sr gives $G_0 = 415$, using Eq. (1) of Vicente et al. (2013) with a standard [C]/[H] $\sim 10^{-4}$ and 4% of elemental carbon locked in PAHs (Tielens 2005). All estimates are consistent with each other, and with irradiation by the Trapezium cluster at a projected separation of $\sim$2 pc. We adopt the middle ground: $G_0 = 415$.

The resulting abundance profiles of gas-phase HCl, Cl, Cl$^+$ and H$_2$Cl$^+$ are shown in the left-hand panel of Fig. 10. For both ζ values, HCl peaks at $\sim 10^{-8}$ at the H/H$_2$ transition, then decreases deeper into the PDR. By $A_V \approx 1$, $X(HCl)_{gas}$ drops
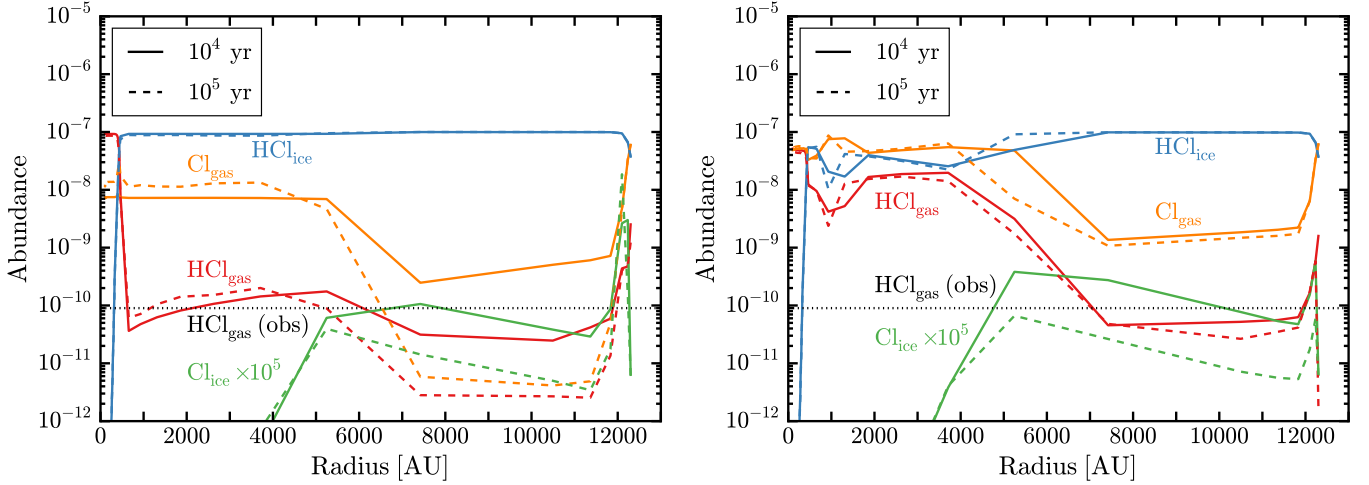
---

[4] http://pdr.obspm.fr/PDRcode.html

Fig. 9. HCl and Cl gas- and ice-phase abundances by 10^4 (solid) and 10^5 yr (dashed) after the dark cloud stage, as modelled with Nautilus. The cosmic ray ionization rate is $\zeta = 10^{-16}$ s^{-1} (*left panel*) and $\zeta = 10^{-14}$ s^{-1} (*right panel*).
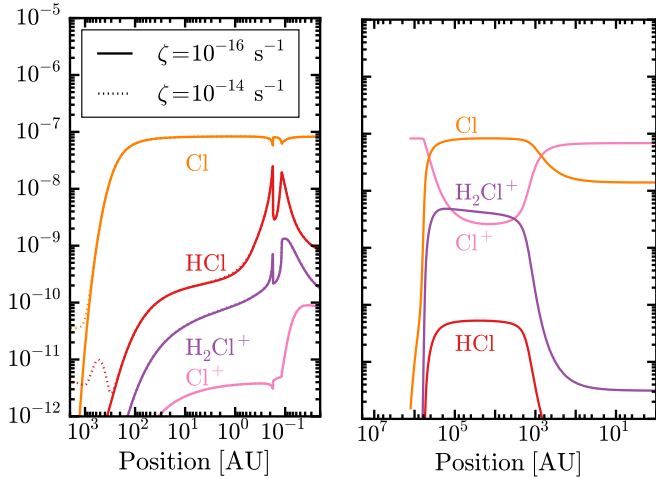

Fig. 10. Meudon models of the chlorine chemistry in the two PDR layers seen towards FIR 4, showing abundances relative to n_{gas}. *Left panel*: dense PDR in the outermost envelope of FIR 4, with $n_{gas} = 6 \times 10^5$ cm^{-3}, $G_0 = 415$ ISRF. The cosmic ray ionization rate is $\zeta = 10^{-16}$ s^{-1} (solid lines) and $\zeta = 10^{-14}$ s^{-1} (dotted). The position is given outside-in from the right. *Right panel*: tenuous PDR in the foreground of FIR 4, with $n_{gas} = 10^2$ cm^{-3}, $G_0 = 1500$ ISRF and $\zeta = 3 \times 10^{-16}$ s^{-1}. The position is given from the strongly irradiated side *on the right*.

below 10^{-10}. The HCl abundance in these models is different from the Nautilus results because of different initial conditions and because the Meudon code solves for steady state, which the time-dependent Nautilus models do not reach by 10^5 yr. The rapid changes around 0.1 to 0.2 AU are due to numerical issues related to H$_2$ formation and the heating-cooling balance. The effect on HCl is limited to $\lesssim 40\%$ of the column density, and does not substantially affect our conclusions. The temperature in this region is between ~ 100 and ~ 1000 K, and the total column density in the outer PDR is N(HCl) $\approx 1 \times 10^{12}$ cm^{-2}.

Using the X(HCl) profile shown in Fig. 10 for the outermost envelope, we re-fitted the HCl abundance model from Sect. 5.2. The two X(HCl) profiles were joined at $T_{kin} = 25$ K. The impact of the PDR on the HCl emission is small. The best-fit combined model – $X_c = 7 \times 10^{-11}$, $R_{bn} = 9000$ AU – has a reduced

Table 3. Observational results and model predictions for H$_2$Cl$^+$ in the tenuous foreground PDR.

	N [10^{14} cm^{-2}]	T_{ex} [K]	v_{lsr}[km s^{-1}]	δv [km s^{-1}]
Observed	1.3 ± 0.1	4.3 ± 0.1	9.3 ± 0.1	1.8 ± 0.1
Modelled	0.11	–	–	–

Notes. Dashes are quantities not obtainable from the chemical model. See Sect. 6 for details.

$\chi^2 = 1.55$. The model matches a tentative narrow peak in the HCl 2–1 line, which the constant abundance model does not, although this does not improve the global χ^2.

In the outer envelope PDR, elemental chlorine is not depleted from the gas in the outermost 300 AU. The PDR model is consistent with the observed HCl emission, and still requires most of the narrow and broad HCl flux to originate deeper in FIR 4. It is also consistent with the upper limit on H$_2$Cl$^+$ absorption at 11.4 km s^{-1}. The H$_2$Cl$^+$ data is analysed next, in Sect. 6.

6. Analysis of H$_2$Cl$^+$

The H$_2$Cl$^+$ lines, shown in Fig. B.1, appear in absorption against the weak continuum of the source. As shown in Fig. 3, they are blueshifted by 2 km s^{-1} with respect to the systemic velocity of FIR 4, which is 11.4 km s^{-1}. Thus, the H$_2$Cl$^+$ absorption does not originate in the dense outer envelope PDR. Instead, the radial velocity matches that of the tenuous foreground PDR layer recently identified towards FIR 4 by López-Sepulcre et al. (2013a). The distance and relation between the foreground layer and FIR 4 are poorly constrained.

We used the CASSIS[5] software to perform Markov Chain Monte Carlo fitting of local thermodynamic equilibrium models to the H$_2$Cl$^+$ and H$_2^{37}$Cl$^+$ lines. Not all the lines are detected, but are still useful as constraints. To minimize baseline issues, we added the continuum fit of Kama et al. (2013) to baseline subtracted spectra. We find a column density of N(H$_2$Cl$^+$) = 1.3×10^{14} and an isotopic ratio of [^{35}Cl]/[^{37}Cl] = (4.3 ± 0.8). The main fitting results are given in Table 3.

---

[5] http://cassis.irap.omp.eu

To compare the observed H_2Cl^+ column density with that expected from the chlorine chemical network, we again used the Meudon code (Le Petit et al. 2006). The foreground PDR was determined by López-Sepulcre et al. (2013a) to have a density of $n = 10^2$ cm^{-3}, an FUV irradiation of $\sim$1500 G_0 and a cosmic ray ionization rate of 3×10^{-16} s^{-1}. The resulting abundance profiles of Cl, Cl$^+$, HCl and H_2Cl^+ are shown in the right-hand panel of Fig. 10. The PDR chemistry model predicts $N(H_2Cl^+) = 1.1 \times 10^{13}$ cm^{-2}, an order of magnitude below the observed value.

An order of magnitude excess of the observed H_2Cl^+ column density over the chemical model predictions, such as we find for FIR 4, has been noted since the recent first identification of the species towards NGC 6334I and Sgr B2(S) by Lis et al. (2010), who suggested viewing geometry as a possible explanation – PDR model column densities are commonly given for a face-on viewing angle. The discrepancy was discussed in detail for several sources by Neufeld et al. (2012), but no satisfactory explanation surfaced, although suggestions for future work were given by the authors in their Sect. 6. Thus, while our data is consistent with no depletion of chlorine from the gas in the tenuous foreground layer, evidently our understanding either of chlorine in diffuse PDRs or of the geometry and conditions in these regions, is not yet complete.

7. Discussion

7.1. Depletion of chlorine

We find a ratio of elemental volatile chlorine to gas-phase HCl, $X(Cl)_{tot}/X(HCl)_{gas}$, of $\sim$1000 in FIR 4. Previous studies of the HCl abundance in molecular gas have found ratios in the range 50 to 640, typically $\sim$400 (e.g. Schilke et al. 1995; Zmuidzinas et al. 1995; Salez et al. 1996; Neufeld & Green 1994; Peng et al. 2010). A depletion factor of $\sim$100 was found for the outflow-shocked region L1157-B1 (Codella et al. 2012).

Our modelling suggests that hydrogen chloride ice is the main chlorine reservoir in protostellar core conditions, containing 90 to 98% of the elemental volatile chlorine. Gas-phase atomic Cl contains most of the remaining 10% of the chlorine.

The above result is independent of our choice of cosmic ray ionization rate, ζ, although inside of $\sim$5000 AU, the gas-phase abundance of HCl (a minor, but key part in the chlorine budget) can vary substantially depending on this parameter. For $\zeta = 10^{-16}$ s^{-1}, the gaseous HCl abundance stays similar to that of the outer envelope ($\sim$10^{-10}), however for $\zeta = 10^{-14}$ s^{-1} it is 10^{-8} up to 10^5 yr. This is, at face value, not consistent with our observations, as it would cause extremely strong HCl emission which is not observed. On the other hand, evolving the static $\zeta = 10^{-14}$ s^{-1} model beyond 10^5 yr leads to a decreasing abundance of HCl in the gas, and it eventually falls below 10^{-10} in the inner envelope.

Another possibility is that infall influences the abundances in the inner envelope, keeping more chlorine in HCl ice than is seen in our static models. This may require quite rapid infall (within a few thousand years on 5000 AU scales) in order to prevent the buildup of a high gas-phase abundance. The poorly known physical structure on $\lesssim$2000 AU scales also impacts our modelling of the chemistry as well as the excitation of HCl, leading to further uncertainty about the HCl abundance on small scales. Another possibility is that HCl is liberated from grain mantles more slowly than the bulk ice. This might also explain the low gas-phase HCl abundance found in the L1157-B1 shock by (Codella et al. 2012), and would point to some – as yet unknown – relatively refractory reservoirs of chlorine on grains.

The dominance of HCl ice as a reservoir of volatile Cl warrants a discussion of the relevant grain surface processes. Much chlorine arrives on ice mantles in atomic form, rather than already in HCl, and then subsequently reacts with H to form HCl. Chlorine may also react with H_2 also present on an interstellar grain surface, as the barrier for reaction with H_2 is measured to be only 2300 K in the gas phase. On a grain surface, H_2 can tunnel through a barrier of up to 4700 K (Tielens & Hagen 1982). In this way, Cl will act similarly to OH, which also has a low barrier for reaction with H_2 and theory and experiments have shown that that reaction is key to interstellar H_2O formation (Tielens & Hagen 1982; Oba et al. 2012).

Analogous to water solutions of hydrochloric acid, and given the low elemental abundance of chlorine, adsorbed HCl can solvate as a trace ion pair (Cl$^-$ and H_3O^+, e.g. Horn et al. 1992). Theoretical studies suggest this process is energetically allowed on an ice surface and proceeds rapidly by tunnelling at 190 K (Robertson & Clary 1995). Experimental studies show that HCl adsorbs dissociatively at sub-monolayer coverages onto the surface of dense amorphous solid water at temperatures as low as 20 K (Ayotte et al. 2011). As dangling OH bonds are involved – which will be omnipresent on growing interstellar ice surfaces – and in view of the long interstellar timescales, we consider solvation likely on a 10 K icy interstellar grain. Observationally, it is well established that ion-solvation is a key aspect of interstellar ices (Demyk et al. 1998) and experiments have shown that ion-solvation can occur at low temperatures and is promoted by the presence of strong bases such as NH_3, leading to trapped Cl$^-$–NH_4^+ ion pairs (Grim et al. 1989). Dipole alignment in ice mantles can further assist in ion-solvation (Balog et al. 2011).

Upon warmup, HCl will evaporate close to the H_2O evaporation temperature. This likely involves the relaxation of the water ice matrix, followed by the recombination and evaporation of HCl (Olanrewaju et al. 2011). The observed depth of depletion outside of the hot core in FIR 4 is consistent with such a codesorption scenario, although with the present data we can only place an upper limit of 10^{-8} on the gas-phase HCl abundance in the $\sim$500 AU size hot core (or 10^{-7} within 100 AU).

7.2. Uncertainty in the source luminosity

The 1000 $L_\odot$ luminosity of the FIR 4 source model from C09 exceeds the protostellar luminosity of 100 $L_\odot$ found by Furlan et al. (2014, F14). The latter authors, as well as López-Sepulcre et al. (2013b), attribute this to the lower spatial resolution data and larger photometric annuli used by C09. We assess here the potential impact on our results.

While the far-infrared fluxes of C09 were likely contaminated by the nearby source, FIR 3, the (sub-)mm continuum maps were spatially resolved on a scale comparable to that studied by F14 and must be reproduced by any model. For a luminosity and thus cooling rate decrease of 1 dex, the corresponding dust temperature decrease is a factor of 1.5 or $\sim$30%. The fixed mm flux demands a matching increase in the density of the emission region. Recalculating the HCl 1–0 excitation for these conditions implies a change in our derived HCl abundance by at most a factor of two.

The impact of the changed source luminosity on the chemistry is also expected to be small. Lowered temperatures would most of all assist in keeping chlorine locked in ices.

Table 4. $[^{35}Cl]/[^{37}Cl]$ determinations towards the Orion star forming region. All uncertainties are 1σ.

Source/Region	$[^{35}Cl]/[^{37}Cl]$	Notes
OMC-2 FIR 4 (HCl)	3.2 ± 0.1	this work
OMC-2 foreground (H_2Cl^+)	4.3 ± 0.8	this work
OMC-1 position 1	$2.3^{+1.8}_{-0.8}$	Peng et al. (2010)
OMC-1 position 2	$2.5^{+0.9}_{-0.7}$	Peng et al. (2010)
OMC-1	$6.5^{+2.2}_{-2.2}$	Salez et al. (1996)
Orion Bar	$2.1^{+0.5}_{-0.5}$	Peng et al. (2010)
solar system	3.1	Lodders (2003)

7.3. The broad component

The broad component has a combination of relatively large line width (~ 10 km s^{-1}) and large spatial extent (thousands of AU), while embedded in, or at least projected over, a dense protostellar core. As we discuss below, it is not obvious what the nature of this component is. Kinematical evidence relates the broad HCl component to the CS molecule, mapping of which in turn suggests that this component is extended on a scale of $\gtrsim 2100$ AU. Our constant HCl abundance models suggest a best-fit spherically symmetric radial extent of 7000 AU. At first glance, such a large line width and large spatial scale make hypotheses other than an outflow seem unlikely.

There is indeed mounting evidence from kinematical and excitation considerations that FIR 4 indeed hosts a compact outflow (Kama et al. 2013, and in prep.; Furlan et al. 2014). Spatially and spectrally resolved data, to be presented in a companion paper, suggest that the outflow axis runs roughly north to south, with lobe sizes of at a few thousand AU. However, the C^{34}S map in Fig. 4 shows a significant east-west elongation, which seems difficult to explain with such an outflow, unless outflow-driven gas is spilling over the protostellar core surface where the outflow cone breaks out. The C^{34}S velocity map shows a slow rotation around the north-south axis, with a typical velocity an order of magnitude below the linewidth.

It has been proposed that a larger outflow from the nearby Class I source, OMC-2 FIR 3, impacts and shocks the FIR 4 core (Shimajiri et al. 2008). It seems unlikely, however, that the FIR 3 outflow is responsible for the broad line emission in FIR 4, because the broad C^{34}S emission peaks on-source, and because the high-velocity wings of the CO and H$_2$O lines in FIR 4 are perfectly symmetric around the local v_{lsr}. Spatially resolved studies of the high velocity wings of CO are needed to clarify the issue. Previous interferometric observations have had insufficient sensitivity to probe the outflow gas at several tens of km s^{-1}.

7.4. The chlorine isotopic ratio

Studies of this ratio throughout the Galaxy have typically been consistent with the solar system value of 3.1 (Lodders 2003), within large error bars (e.g. Salez et al. 1996; Peng et al. 2010; Cernicharo et al. 2010).

Because of the very small Cl isotope mass difference (6%), minimal chemical fractionation is expected, and we determined the isotope ratio via the HCl and H$_2$Cl$^+$ isotopolog ratios. For HCl, we find a line flux ratio of 3.2 ± 0.1, which is a robust isotopolog ratio indicator, given the low optical depth of the lines suggested by the hyperfine component ratios of the narrow HCl emission (see also Cernicharo et al. 2010). For H$_2$Cl$^+$, we found a ratio of 4.3 ± 0.8. The results, summarized in Table 4, are

consistent with the solar system value and with values measured elsewhere in the Orion star forming region.

7.5. Impact of the new HCl-H$_2$ excitation rates

That the difference between the HCl-H$_2$ excitation rate coefficients and the scaled HCl-He ones should impact abundance determinations was noted already by Lanza et al. (2014b). As shown in Fig. 6, the new HCl-H$_2$ hyperfine-resolved collisional excitation rates are roughly a factor of five to ten larger than the previously used, mass-scaled HCl-He rates from Neufeld & Green (1994) and Lanza & Lique (2012). This suggests that previous estimates of the gas-phase HCl abundance in molecular gas must be re-evaluated to be up to an order of magnitude lower, and correspondingly the typical fraction of elemental chlorine in gas-phase HCl must be around a factor of 10^{-3} (a depletion factor of ~ 1000). Modelling results in Sect. 5.3 show that the strong depletion can be well understood in a framework where elemental chlorine is sequestered into HCl ice, where it remains at least as strongly bound as H$_2$O itself.

Based on the new excitation rates, the critical density of the HCl 1–0 transition is $\sim 10^7$ cm^{-3}. This is accurate within a factor of a few in the temperature range of the new rate coefficients (up to 300 K).

8. Conclusions

We carried out a study of chlorine towards the OMC-2 FIR 4 protostellar core, using *Herschel* and CSO observations of HCl and H$_2$Cl$^+$. Our main findings are listed below.

1. We detect the HCl $1-0$ and $2-1$ transitions in emission with *Herschel* and CSO, and H$_2$Cl$^+$ in absorption with *Herschel*.
2. The narrow HCl component (*FWHM* = 2.0 km s^{-1}) traces the outer envelope, and the broad one (*FWHM* = 10.5 km s^{-1}) a compact central region, possibly outflow-driven gas.
3. The HCl data are well modelled with a constant abundance of $X(\text{HCl})_{\text{gas}} = 9 \times 10^{-11}$ in FIR 4, corresponding to $\sim 10^{-3}$ of the ISM abundance of elemental chlorine.
4. Chemical models show that HCl ice contains ~ 90 to 98% of all volatile chlorine in the source. The second largest reservoir is gas-phase atomic Cl, up to 10% of the total. All other species have much lower abundances. In the inner 100 AU, HCl gas may hold up to 100% of volatile chlorine.
5. The external irradiation of the FIR 4 envelope is $G_0 = 415$ ISRF. Elemental chlorine is undepleted in the outermost 300 AU of the resulting dense PDR. Including this PDR in the source model gives a best-fit $X(\text{HCl})_{\text{gas}} = 7 \times 10^{-11}$ in the rest of the source.
6. H$_2$Cl$^+$ traces a recently discovered diffuse, blueshifted foreground PDR. The observed H$_2$Cl$^+$ column density is 1.3×10^{14} cm^{-2}, an order of magnitude above the model prediction of 1.1×10^{13} cm^{-2}.
7. Our best estimate of the $[^{35}Cl]/[^{37}Cl]$ isotope ratio in OMC-2 FIR 4 is 3.2 ± 0.1 (1σ), consistent with other measurements in the solar system and in the Orion region.
8. Newly calculated HCl-H$_2$ hyperfine-resolved collisional excitation rate coefficients exceed previous HCl-He scaled values by up to an order of magnitude at protostellar core temperatures, suggesting that previous estimates of chlorine depletion from the gas should be revisited.

References

Adams, J. D., Herter, T. L., Osorio, M., et al. 2012, ApJ, 749, L24
Alexander, M. 1979, J. Chem. Phys., 71, 1683
Asplund, M., Grevesse, N., Sauval, A. J., & Scott, P. 2009, ARA&A, 47, 481
Ayotte, P., Marchand, P., Daschbach, J. L., Smith, R. S., & Kay, B. D. 2011, J. Phys. Chem. A, 115, 6002
Bacmann, A., Lefloch, B., Ceccarelli, C., et al. 2002, A&A, 389, L6
Balog, R., Cicman, P., Field, D., et al. 2011, J. Phys. Chem. A, 115, 6820
Bergin, E. A., & Langer, W. D. 1997, ApJ, 486, 316
Blake, G. A., Masson, C. R., Phillips, T. G., & Sutton, E. C. 1986, ApJS, 60, 357
Caselli, P., & Ceccarelli, C. 2012, A&ARv, 20, 56
Caselli, P., Walmsley, C. M., Tafalla, M., Dore, L., & Myers, P. C. 1999, ApJ, 523, L165
Ceccarelli, C., Bacmann, A., Boogert, A., et al. 2010, A&A, 521, L22
Ceccarelli, C., Caselli, P., Bockelee-Morvan, D., et al. 2014, in Protostars and Planets VI, eds. H. Beuther, R. S. Klessen, C. P. Dullemond, & T. Henning (Tucson: University of Arizona Press), 859
Cernicharo, J., Goicoechea, J. R., Daniel, F., et al. 2010, A&A, 518, L115
Codella, C., Ceccarelli, C., Bottinelli, S., et al. 2012, ApJ, 744, 164
Collings, M. P., Anderson, M. A., Chen, R., et al. 2004, MNRAS, 354, 1133
Crimier, N., Ceccarelli, C., Lefloch, B., & Faure, A. 2009, A&A, 506, 1229
Dalgarno, A., de Jong, T., Oppenheimer, M., & Black, J. H. 1974, ApJ, 192, L37
de Graauw, T., Helmich, F. P., Phillips, T. G., et al. 2010, A&A, 518, L6
Demyk, K., Dartois, E., D'Hendecourt, L., et al. 1998, A&A, 339, 553
Dubernet, M.-L., Alexander, M. H., Ba, Y. A., et al. 2013, A&A, 553, A50

Faure, A., & Lique, F. 2012, MNRAS, 425, 740
Furlan, E., Megeath, S. T., Osorio, M., et al. 2014, ApJ, 786, 26
Grim, R. J. A., Greenberg, J. M., de Groot, M. S., et al. 1989, A&AS, 78, 161
Guillon, G., & Stoecklin, T. 2012, MNRAS, 420, 579
Herrmann, F., Madden, S. C., Nikola, T., et al. 1997, ApJ, 481, 343
Hersant, F., Wakelam, V., Dutrey, A., Guilloteau, S., & Herbst, E. 2009, A&A, 493, L49
Hincelin, U., Wakelam, V., Hersant, F., et al. 2011, A&A, 530, A61
Hirota, T., Bushimata, T., Choi, Y. K., et al. 2007, PASJ, 59, 897
Hogerheijde, M. R., & van der Tak, F. F. S. 2000, A&A, 362, 697
Horn, A. B., Chesters, M. A., McCoustra, M. R. S., & Sodeau, J. R. 1992, J. Chem. Soc., Faraday Trans., 88, 1077
Jørgensen, J. K., Schöier, F. L., & van Dishoeck, E. F. 2005, A&A, 435, 177
Jura, M. 1974, ApJ, 190, L33
Kama, M., Dominik, C., Maret, S., et al. 2010, A&A, 521, L39
Kama, M., López-Sepulcre, A., Dominik, C., et al. 2013, A&A, 556, A57
Lanza, M., & Lique, F. 2012, MNRAS, 424, 1261
Lanza, M., Kalugina, Y., Wiesenfeld, L., Faure, A., & Lique, F. 2014a, MNRAS, submitted
Lanza, M., Kalugina, Y., Wiesenfeld, L., & Lique, F. 2014b, J. Chem. Phys., 140, 064316
Lattelais, M., Bertin, M., Mokrane, H., et al. 2011, A&A, 532, A12
Le Petit, F., Nehmé, C., Le Bourlot, J., & Roueff, E. 2006, ApJS, 164, 506
Lee, H.-H., Herbst, E., Pineau des Forets, G., Roueff, E., & Le Bourlot, J. 1996, A&A, 311, 690
Lis, D. C., Pearson, J. C., Neufeld, D. A., et al. 2010, A&A, 521, L9
Lodders, K. 2003, ApJ, 591, 1220
López-Sepulcre, A., Kama, M., Ceccarelli, C., et al. 2013a, A&A, 549, A114
López-Sepulcre, A., Taquet, V., Sánchez-Monge, Á., et al. 2013b, A&A, 556, A62
Manoj, P., Watson, D. M., Neufeld, D. A., et al. 2013, ApJ, 763, 83
Menten, K. M., Reid, M. J., Forbrich, J., & Brunthaler, A. 2007, A&A, 474, 515
Mezger, P. G., Zylka, R., & Wink, J. E. 1990, A&A, 228, 95
Moomey, D., Federman, S. R., & Sheffer, Y. 2012, ApJ, 744, 174
Neufeld, D. A., & Green, S. 1994, ApJ, 432, 158
Neufeld, D. A., & Wolfire, M. G. 2009, ApJ, 706, 1594
Neufeld, D. A., Roueff, E., Snell, R. L., et al. 2012, ApJ, 748, 37
Novotný, O., Buhr, H., Hamberg, M., et al. 2012, in IOP Publishing, 62047
Oba, Y., Watanabe, N., Hama, T., et al. 2012, ApJ, 749, 67
Olanrewaju, B. O., Herring-Captain, J., Grieves, G. A., Aleksandrov, A., & Orlando, T. M. 2011, J. Phys. Chem. A, 115, 5936
Ott, S. 2010, in Astronomical Data Analysis Software and Systems XIX, eds. Y. Mizumoto, K.-I. Morita, & M. Ohishi, ASP Conf. Ser., 434, 139
Peng, R., Yoshida, H., Chamberlin, R. A., et al. 2010, ApJ, 723, 218
Pilbratt, G. L., Riedinger, J. R., Passvogel, T., et al. 2010, A&A, 518, L1
Robertson, S. H., & Clary, D. C. 1995, Faraday Discuss., 100, 309
Roueff, E., & Lique, F. 2013, Chem. Rev., 113, 8906
Salez, M., Frerking, M. A., & Langer, W. D. 1996, ApJ, 467, 708
Schilke, P., Phillips, T. G., & Wang, N. 1995, ApJ, 441, 334
Schöier, F. L., van der Tak, F. F. S., van Dishoeck, E. F., & Black, J. H. 2005, A&A, 432, 369
Semenov, D., Hersant, F., Wakelam, V., et al. 2010, A&A, 522, A42
Shimajiri, Y., Takahashi, S., Takakuwa, S., Saito, M., & Kawabe, R. 2008, ApJ, 683, 255
Tielens, A. G. G. M. 2005, The Physics and Chemistry of the Interstellar Medium (Cambridge: Cambridge University Press)
Tielens, A. G. G. M., & Hagen, W. 1982, A&A, 114, 245
Vicente, S., Berné, O., Tielens, A. G. G. M., et al. 2013, ApJ, 765, L38
Wakelam, V., Herbst, E., Loison, J.-C., et al. 2012, ApJS, 199, 21
Zmuidzinas, J., Blake, G. A., Carlstrom, J., Keene, J., & Miller, D. 1995, ApJ, 447, L125

Appendix A: Hyperfine excitation of HCl by H₂

Rate coefficients for rotational excitation of HCl($^1\Sigma^+$) by collisions with H₂ molecules have been computed by Lanza et al. (2014a) for temperatures ranging from 5 to 300 K. The rate coefficients were derived from extensive quantum calculations using a new accurate potential energy surface obtained from highly correlated ab initio approaches (Lanza et al. 2014b).

However, in these calculations, the hyperfine structure of HCl was neglected. To model the spectrally resolved HCl emission from molecular clouds, hyperfine resolved rate coefficients are needed. In this appendix, we present the calculations of HCl–H₂ hyperfine resolved rate coefficients from the rotational rate coefficients of Lanza et al. (2014a). Note that, for rotational levels, we use here the lowercase j instead of the astronomical J notation used in the main body of the paper.

A.1. Methods

In HCl, the coupling between the nuclear spin ($I_1 = 3/2$) of the chlorine atom and the molecular rotation results in a weak splitting of each rotational level j_1 into 4 hyperfine levels (except for the $j_1 = 0$ level which is split into only 1 level and for the $j_1 = 1$ level which is split into only 3 levels). Each hyperfine level is designated by a quantum number F_1 ($F_1 = I_1 + j_1$) varying between $|I_1 - j_1|$ and $I_1 + j_1$. In the following, j_2 designates the rotational momentum of the H₂ molecule.

In order to get HCl–H₂ hyperfine resolved rate coefficients, we extend the Infinite Order Sudden (IOS) approach for diatom-atom collisions (Faure & Lique 2012) to the case of diatom-diatom collisions.

Within the IOS approximation, inelastic rotational rate coefficients $k^{IOS}_{j_1,j_2 \to j'_1,j'_2}(T)$ can be calculated from the "fundamental" rates (those out of the lowest $j_1 = 0, j_2 = 0$ channel) as follows (e.g. Alexander 1979):

$$k^{IOS}_{j_1,j_2 \to j'_1,j'_2}(T) = \sum_{L_1,L_2}(2j'_2 + 1)(2j'_1 + 1)\begin{pmatrix} j_1 & L_1 & j'_1 \\ 0 & 0 & 0 \end{pmatrix}^2$$
$$\times \begin{pmatrix} j_2 & L_2 & j'_2 \\ 0 & 0 & 0 \end{pmatrix}^2 k^{IOS}_{0,0 \to L_1,L_2}(T). \tag{A.1}$$

Similarly, IOS rate coefficients amongst hyperfine structure levels can be obtained from the $k^{IOS}_{0,0 \to L_1,L_2}(T)$ rate coefficients using the following formula:

$$k^{IOS}_{j_1,F_1,j_2 \to j'_1,F'_1,j'_2}(T) = \sum_{L_1,L_2}(2j'_2 + 1)(2j_1 + 1)(2j'_1 + 1)$$
$$\times(2F'_1 + 1)\begin{pmatrix} j_2 & L_2 & j'_2 \\ 0 & 0 & 0 \end{pmatrix}^2\begin{pmatrix} j'_1 & j_1 & L_1 \\ 0 & 0 & 0 \end{pmatrix}^2$$
$$\times \begin{Bmatrix} L_1 & F_1 & F'_1 \\ I_1 & j'_1 & j_1 \end{Bmatrix}^2 k^{IOS}_{0,0 \to L_1,L_2}(T) \tag{A.2}$$

where ( ) and { } are respectively the "$3 - j$" and "$6 - j$" Wigner symbols.

The IOS approximation is expected to be moderately accurate at low temperature. As suggested by Neufeld & Green (1994), we could improve the accuracy by computing the hyperfine rate coefficients as:

$$k^{SIOS}_{j_1,F_1,j_2 \to j'_1 F'_1,j'_2}(T) = \frac{k^{IOS}_{j_1,F_1,j_2 \to j'_1,F'_1,j'_2}(T)}{k^{IOS}_{j_1,j_2 \to j'_1,j'_2}(T)}k^{CC}_{j_1,j_2 \to j'_1,j'_2}(T) \tag{A.3}$$
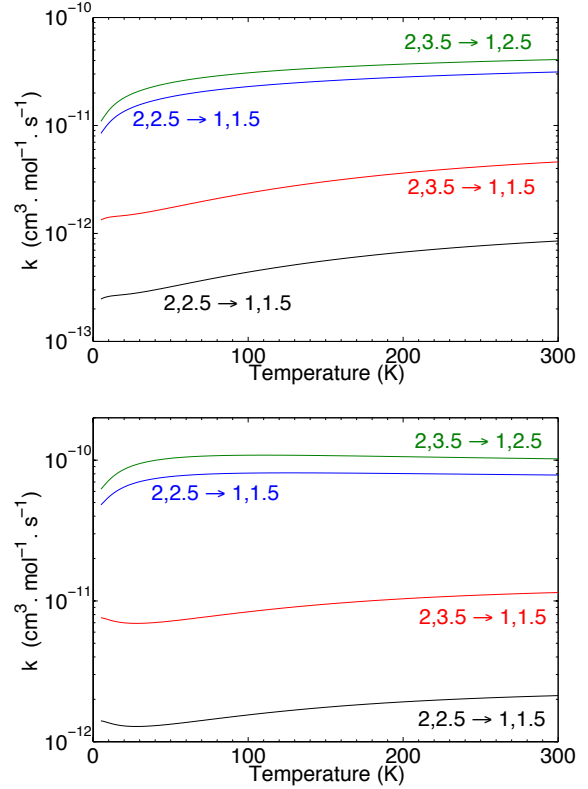

Fig. A.1. Temperature dependence of the hyperfine resolved HCl–para-H₂ (*upper panel*) and HCl–ortho-H₂ (*lower panel*) rate coefficients for HCl($j_1 = 2, F \to j'_1 = 1, F'$) transitions.

using the CC rate coefficients $k^{CC}_{0,0 \to L_1,L_2}(T)$ of Lanza et al. (2014a) for the IOS "fundamental" rates in Eqs. (A.1)–(A.2). $k^{CC}_{j_1,j_2 \to j'_1,j'_2}(T)$ are the rotational rate coefficients also taken from Lanza et al. (2014a). We named the method "SIOS" for scaled IOS.

In addition, fundamental excitation rates $k^{CC}_{0,0 \to L_1,L_2}(T)$ were replaced by the de-excitation fundamental rates using the detailed balance relation:

$$k^{CC}_{0,0 \to L_1,L_2}(T) = (2L_1 + 1)(2L_2 + 1)k^{IOS}_{L_1,L_2 \to 0,0}(T). \tag{A.4}$$

This procedure is found to significantly improve the results at low temperature due to important threshold effects.

Hence, we have determined hyperfine HCl–H₂ rate coefficients using the computational scheme described above for temperature ranging from 5 to 300 K. We considered transitions between the 28 first hyperfine levels of HCl ($j, j' \leq 7$) due to collisions with para-H₂ ($j_2 = 0$) and ortho-H₂ ($j_2 = 1$). The present approach has been shown to be accurate, even at low temperature, and has also been shown to induce almost no inaccuracies in radiative transfer modeling compared to more exact calculations of the rate coefficients (Faure & Lique 2012).

A.2. Results

The complete set of (de)excitation rate coefficients is available on-line from the LAMDA[6] (Schöier et al. 2005) and BASECOL[7] (Dubernet et al. 2013) websites. For illustration, Fig. A.1 depicts

---

[6] http://www.strw.leidenuniv.nl/~moldata/
[7] http://basecol.obspm.fr/

Table A.1. A comparison between present hyperfine rate coefficients for ortho- and para-H$_2$, and those of LL12 for He.

$j_1, F_1 \rightarrow j'_1, F'_1$	10 K			100 K			300 K		
	p-H$_2$	o-H$_2$	He × 1.38	p-H$_2$	o-H$_2$	He×1.38	p-H$_2$	o-H$_2$	He × 1.38
1, 1.5 → 0, 1.5	5.54e-11	1.53e-10	3.97e-12	6.99e-11	1.53e-10	1.99e-11	5.19e-11	1.13e-10	3.45e-11
2, 2.5 → 0, 1.5	2.01e-11	3.33e-11	2.64e-12	2.31e-11	5.07e-11	8.82e-12	2.53e-11	6.15e-11	2.40e-11
2, 3.5 → 1, 1.5	1.41e-12	7.35e-12	3.38e-12	2.37e-12	8.37e-12	3.35e-12	4.60e-12	1.15e-11	3.55e-12
2, 3.5 → 1, 2.5	1.38e-11	7.17e-11	1.54e-11	3.07e-11	1.08e-10	2.65e-11	4.08e-11	1.02e-10	4.27e-11
3, 3.5 → 0, 1.5	9.31e-12	1.08e-11	2.28e-12	8.72e-12	1.05e-11	3.06e-12	9.65e-12	1.16e-11	3.59e-12
3, 3.5 → 1, 1.5	6.28e-12	1.58e-11	2.04e-12	8.62e-12	2.47e-11	6.66e-12	1.39e-11	3.73e-11	1.92e-11
3, 2.5 → 1, 1.5	5.90e-12	1.48e-11	1.59e-12	8.07e-12	2.31e-11	5.56e-12	1.28e-11	3.42e-11	1.69e-11
3, 2.5 → 2, 3.5	3.85e-13	2.27e-12	1.45e-12	7.31e-13	3.13e-12	2.32e-12	2.37e-12	6.32e-12	6.15e-12
3, 4.5 → 2, 2.5	4.56e-13	2.69e-12	1.84e-12	8.05e-13	3.44e-12	2.29e-12	2.51e-12	6.65e-12	3.99e-12

Notes. The rates are in units of cm^3 mol^{-1} s^{-1}.

the evolution of para- and ortho-H$_2$ rate coefficients as a function of temperature for HCl($j = 2, F \rightarrow j' = 1, F'$) transitions.

First of all and as already discussed in Lanza et al. (2014a), para- and ortho-H$_2$ rate coefficients differ significantly, the rate coefficients being larger for ortho-H$_2$ collisions. One can also clearly see that there is a strong propensity in favour of $\Delta j_1 = \Delta F_1$ transitions for both collisions with para- and ortho-H$_2$. This trend is the usual trend for such a molecule (Roueff & Lique 2013).

Finally, we compare in Table A.1 our new hyperfine HCl–H$_2$ rate coefficients with the HCl–He ones calculated by Lanza & Lique (2012) which are scaled by a factor 1.38 to account for the mass difference (see Fig. 6 for a visual comparison).

Indeed, collisions with helium are often used to model collisions with *para*-H$_2$. It is generally assumed that rate coefficients with *para*-H$_2$($j_2 = 0$) should be larger than He rate coefficients owing to the smaller collisional reduced mass.

As one can see, the scaling factor is clearly different from 1.38. The ratio varies with the transition considered and also with the temperature for a given transition. The ratio may be larger than a factor 10. This comparison indicates that accurate rate coefficients with para-H$_2$ ($j_2 = 0$) and ortho-H$_2$ ($j_2 = 1$) could not be obtained from He rate coefficients. HCl molecular emission analysis performed with HCl-He rate coefficients result in large inaccuracies in the HCl abundance determination.

Appendix B: CASSIS fitting of H_2Cl^+

In Fig. B.1, we show the H_2Cl^+ lines used in the LTE fitting with the CASSIS software and the best-fit model resulting from the χ^2 minimization. The hyperfine components and other lines detected nearby are also shown. The data are all from the HIFI spectral survey of FIR 4 (Kama et al. 2013).
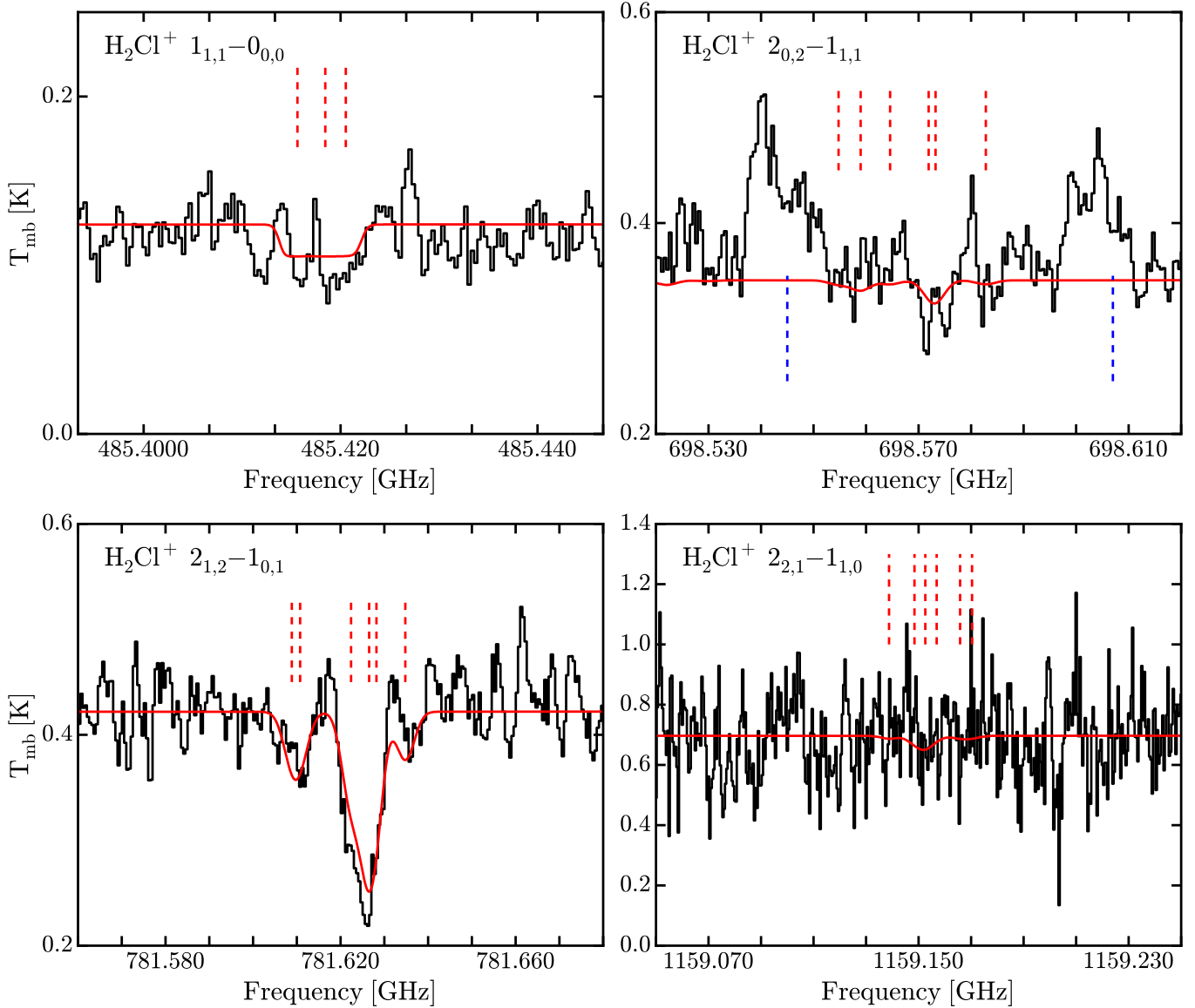

Fig. B.1. The four H_2Cl^+ lines (black) used in the LTE model fitting with CASSIS, and the best-fit model (red). All spectra are corrected for the foreground PDR velocity of 9.4 km s^{-1}. The dashed red lines show the hyperfine components of H_2Cl^+ transitions, while dashed blue lines in the *top right* panel indicate the native frequencies of C_2H transitions. The other H_2Cl^+ transitions do not have any lines nearby that were listed as detections in the spectral survey of Kama et al. (2013).